

Phase separation in a binary mixture confined between symmetric parallel plates: Capillary condensation transition near the bulk critical point

Syunsuke Yabunaka¹, Ryuichi Okamoto², and Akira Onuki¹

¹*Department of Physics, Kyoto University, Kyoto 606-8502*

²*Fukui Institute for Fundamental Chemistry, Kyoto University, Kyoto 606-8103*

(Dated: January 4, 2013)

We investigate phase separation of near-critical binary mixtures between parallel symmetric walls in the strong adsorption regime. We take into account the renormalization effect due to the critical fluctuations using the recent local functional theory [J. Chem. Phys. **136**, 114704 (2012)]. In statics, a van der Waals loop is obtained in the relation between the average order parameter $\langle \psi \rangle$ in the film and the chemical potential when the temperature T is lower than the film critical temperature T_c^{ca} (in the case of an upper critical solution temperature). In dynamics, we lower T below the capillary condensation line from above T_c^{ca} . We calculate the subsequent time-development assuming no mass exchange between the film and the reservoir. In the early stage, the order parameter ψ changes only in the direction perpendicular to the walls. For sufficiently deep quenching, such one-dimensional profiles become unstable with respect to the fluctuations varying in the lateral directions. The late-stage coarsening is then accelerated by the hydrodynamic interaction. A pancake domain of the phase disfavored by the walls finally appears in the middle of the film.

PACS numbers: 64.75.St, 64.70.qj, 68.03.Fg

I. INTRODUCTION

The phase behavior of fluids confined in narrow regions has been studied extensively [1–3]. It strongly depends on the geometry of the walls and on the molecular interactions between the fluid and the walls. Its understanding is crucial in the physics of fluids in porous media. It is also needed to study the dynamics of confined fluids.

In particular, the liquid phase is usually favored by the walls in one-component fluids, while one component is preferentially attracted to the walls in binary mixtures [4–10]. In such situations, narrow regions may be filled with the phase favored by the walls or may hold some fraction of the disfavored phase. Hence, in the film geometry, there appears a first-order phase transition between these states, which forms a line (CCL) ending at a film critical point outside the bulk coexistence curve in the T - μ_∞ plane [1–3, 11–14], where μ_∞ is the reservoir chemical potential [15]. We call it the capillary condensation transition even for binary mixtures, though this name has been used for the gas-liquid phase transition in porous media [2]. Around CCL, the reservoir is rich in the component disfavored by the walls for binary mixtures. With increasing the wall separation D , the film critical point approaches the bulk critical point. Crossover then occurs between two-dimensional (2d) and three-dimensional (3d) phase transition behaviors.

For Ising films near the bulk criticality, Fisher and Nakanishi [11] presented the scaling theory of CCL in the T - h plane, where h represents applied magnetic field. They also calculated CCL in the mean-field ϕ^4 theory. Evans *et al.* used the density functional theory to calculate the inhomogeneous structures in pores [12]. For a Lennard-Jones fluid in cylindrical pores, Peterson *et al.*[13] obtained steady gas-liquid two-phase patterns. For a lattice gas model, Binder and Landau [14] studied

the capillary condensation transition using a Monte Carlo method. For a microscopic model of 2d Ising stripes, Maciołek *et al* [16] found a (pseudo) CCL using a density-matrix renormalization-group method. For square well fluids in slit pores, Singh *et al.*[17] numerically examined the crossover from 3d to 2d.

Recently, two of the present authors [18] calculated CCL near the bulk critical point using the local functional theory [19, 20], which accounts for the renormalization effect due to the critical fluctuations. The lowering of the film critical temperature T_c^{ca} from the bulk critical temperature T_c was shown to be proportional to $D^{-1/\nu}$ (where $\nu \cong 0.63$) in accord with the scaling theory [11]. Along CCL, our calculations [18] and those by Maciołek *et al* [16] showed strong enhancement of the so-called Casimir amplitudes [21]. Similar first-order transitions were found between plates [22] and colloids [23] in binary mixtures containing salt.

The aim of this paper is to investigate the phase separation in near-critical binary mixtures between parallel plates using model H and model B [24, 25]. Here, phase separation takes place around CCL and the hydrodynamic interaction is crucial in the late-stage phase separation. It is worth noting that near-critical fluids in porous media exhibit history-dependent frozen domains and activated dynamics with non-exponential relaxations [26, 27]. To gain insight into such complicated effects, we may start with near-critical fluids in the film geometry. Treating near-critical fluids, we may construct a universal theory with a few materials-independent parameters, where D much exceeds microscopic spatial scales.

In the literature, much attention has been paid to the interplay of wetting and phase separation [28–31], which is referred to as surface-directed phase separation. However, simulations including the hydrodynamic interaction have not been abundant [30, 32–34]. We mention that

Tanaka and Araki [33] integrated the model H equations in the semi-infinite situation and Jaiswal *et al.* [34] performed molecular dynamics simulation to investigate the hydrodynamic flow effect between parallel plates. In our simulation, the order parameter ψ changes in the direction perpendicular to the walls in the strong adsorption regime. Then, the dynamics is one-dimensional in an early stage but the fluid flow in the lateral directions accelerates the late-stage coarsening even under the no-slip boundary condition on the walls [25, 30, 32–34].

On the other hand, Porcheron and Monson [35] numerically studied the dynamics of extrusion and intrusion of liquid mercury between a cylindrical pore and a reservoir. Such a process is crucial in experiments of adsorption and desorption between a porous material and a surrounding fluid [2]. In our simulation we assume no mass exchange imposing the periodic boundary condition in the lateral directions, as in the previous simulations of surface-directed phase separation.

The organization of this paper is as follows. In Sec.II, we will summarize the results of the local functional theory of near-critical binary mixtures in the film geometry. We will newly present some results on the phase behavior, which will facilitate understanding the phase separation near CCL. In Sec.III, we will present our simulation results of the phase separation with the velocity field (model H) and without it (model B).

II. THEORETICAL BACKGROUND

This section provides the theoretical background of our simulation on the basis of our previous paper [18]. The Boltzmann constant k_B will be set equal to unity.

A. Ginzburg-Landau free energy

We suppose near-critical binary mixtures with an upper critical solution temperature (UCST) T_c at a constant pressure. The order parameter ψ is proportional to $c - c_c$, where c is the composition and c_c is its critical value. The reduced temperature is written as

$$\tau = (T - T_c)/T_c. \quad (2.1)$$

In our numerical analysis, the usual critical exponents take the following values[25]:

$$\begin{aligned} \alpha &= 0.110, & \beta &= 0.325, & \gamma &= 1.240, \\ \nu &= 0.630, & \eta &= 0.0317, & \delta &= 4.815. \end{aligned} \quad (2.2)$$

At the critical composition with $\tau > 0$, the correlation length is written as $\xi = \xi_0\tau^{-\nu}$, where ξ_0 is a microscopic length. The coexistence curve in the region $\tau < 0$ is denoted by CX. The correlation length on CX is written as $\xi = \xi'_0|\tau|^{-\nu}$, where ξ'_0 is another microscopic length

with the ratio $R_\xi = \xi_0/\xi'_0$ being a universal number. We write ψ in the coexisting two phases as $\pm\psi_{\text{cx}}$ with

$$\psi_{\text{cx}} = b_{\text{cx}}|\tau|^\beta, \quad (2.3)$$

where b_{cx} is a constant.

We assume that the bulk free energy F including the gradient part is of the local functional form [18–20],

$$F = \int d\mathbf{r}[f + \frac{1}{2}T_cC|\nabla\psi|^2]. \quad (2.4)$$

In the following, we give a simple form for the free energy density $f = f(\psi, \tau)$. In our theory, the critical fluctuations with sizes smaller than the correlation length ξ have already been coarse-grained at the starting point.

B. Coexistence-curve exterior

Outside CX, f is of the Ginzburg-Landau form,

$$f/T_c = \frac{r}{2}\psi^2 + \frac{u}{4}\psi^4. \quad (2.5)$$

Here, we have omitted the free energy contribution for $\psi = 0$, whose singular part is proportional to $|\tau|^{2-\alpha}$ yielding the specific heat singularity. The coefficients r and u in f and C in F are renormalized ones in three dimensions. As in the linear parametric model [36], we use a nonnegative parameter w representing the distance from the critical point in the τ - ψ plane to obtain

$$r/\tau = C_1\xi_0^{-2}w^{\gamma-1}, \quad (2.6)$$

$$u/u^* = C_1^2\xi_0^{-1}w^{(1-2\eta)\nu}, \quad (2.7)$$

$$C = C_1w^{-\eta\nu}, \quad (2.8)$$

where C_1 and u^* are constants. We may set $C_1 = 1$ by rescaling $C_1^{1/2}\psi \rightarrow \psi$ without loss of generality. In the present case, $(C_1\xi_0)^{1/2}\psi$ is dimensionless. The constant u^* is a universal number and we set $u^* = 2\pi^2/9$. The fractional powers of w in Eqs.(2.6)–(2.8) arise from the renormalization of the critical fluctuations with wavenumbers larger than the inverse correlation length ξ^{-1} . We determine w as a function of τ and ψ by

$$w = \tau + (3u^*C_1\xi_0)w^{1-2\beta}\psi^2, \quad (2.9)$$

which is equivalent to $w^\gamma = (r + 3u\psi^2)\xi_0^2/C_1$. Thus, $w = \tau$ for $\psi = 0$ and $\tau \geq 0$, while $|\psi| \propto w^\beta$ for $\tau = 0$.

The derivative $\mu = \partial f/\partial\psi$ at fixed τ denotes the chemical potential difference between the two components[10, 15, 19], but it will be simply called the chemical potential. In terms of the ratio $S = \tau/w$, it reads

$$\frac{\mu}{T_c} = \frac{2 - \alpha + 4(1 - \alpha)S + 5\alpha S^2}{6[2\beta + (1 - 2\beta)S]\xi_0^2}C_1w^\gamma\psi. \quad (2.10)$$

On CX, we require $\mu = 0$, which yields the equation $2 - \alpha + 4(1 - \alpha)S + 5\alpha S^2 = 0$ for S . On CX, this gives

$S = -1/\sigma$ or $w = -\sigma\tau$ with $\sigma = 1.714$. Together with Eqs.(2.3) and (2.9), we obtain

$$b_{cx}^2 = (1 + \sigma)\sigma^{2\beta-1}/3u^*C_1\xi_0. \quad (2.11)$$

We introduce the susceptibility $\chi = \chi(\tau, \psi)$ defined by

$$T_c/\chi = \partial\mu/\partial\psi = \partial^2 f/\partial\psi^2. \quad (2.12)$$

For $\psi = 0$ and $\tau > 0$, we simply obtain $\chi(\tau, 0) = C_1^{-1}\xi_0^2\tau^{-\gamma}$. On CX, we write $\chi_{cx} = \chi(\tau, \psi_{cx})$. In terms of the critical amplitude ratio $R_\chi = \chi(|\tau|, 0)/\chi_{cx}$ for $\tau < 0$, the susceptibility on CX reads

$$\chi_{cx} = R_\chi^{-1}C_1^{-1}\xi_0^2|\tau|^{-\gamma}. \quad (2.13)$$

Some calculations give $R_\chi = 8.82$ [37]. In terms of χ , the correlation length is expressed as $\xi = (C\chi)^{1/2}$, which yields the critical amplitude ratio $R_\xi = \xi_0/\xi'_0 = 2.99$ [37]. For $\tau = 0$, we have $\xi \propto |\psi|^{-\nu/\beta}$.

C. Coexistence-curve interior

The interior of CX is given by $|\psi| < \psi_{cx}$ and $\tau < 0$, where we need to define the free energy density f to examine two-phase coexistence. We assume a ψ^4 -theory with coefficients depending only on τ , where $\partial f/\partial\psi = \mu$ and $\partial^2 f/\partial\psi^2 = T_c/\chi$ are continuous across the coexistence curve. We then obtain

$$(f - f_{cx})/T_c = (\psi_{cx}^2/8\chi_{cx})(\psi^2/\psi_{cx}^2 - 1)^2, \quad (2.14)$$

where f_{cx} is the free energy density on CX and χ_{cx} is defined by Eq.(2.13). We also set

$$C = C_{cx} = C_1|\sigma\tau|^{-\eta\nu}, \quad (2.15)$$

which is the value of C on CX. The renormalization effect inside CX is assumed to be unchanged from that on CX with the same τ . The μ inside CX then reads

$$\mu/T_c = (\psi^2/\psi_{cx}^2 - 1)\psi/2\chi_{cx} \quad (2.16)$$

The surface tension σ between coexisting bulk two phases is given by the standard expression,

$$\begin{aligned} \sigma &= 2T_c(C_{cx}/\chi_{cx})^{1/2}\psi_{cx}^2/3 \\ &= A_s T_c/\xi^2, \end{aligned} \quad (2.17)$$

where $\xi = \xi'_0|\tau|^{-\nu}$ is the correlation length on CX. The universal number A_s is estimated to be 0.075 in our model, while its reliable value is about 0.09 [18].

D. Near-critical fluids between parallel plates

We suppose a near-critical fluid between parallel symmetric walls in the region $0 < z < D$, where D is much longer than any microscopic lengths. To avoid the discussion of the edge effect, the lateral plate dimension L

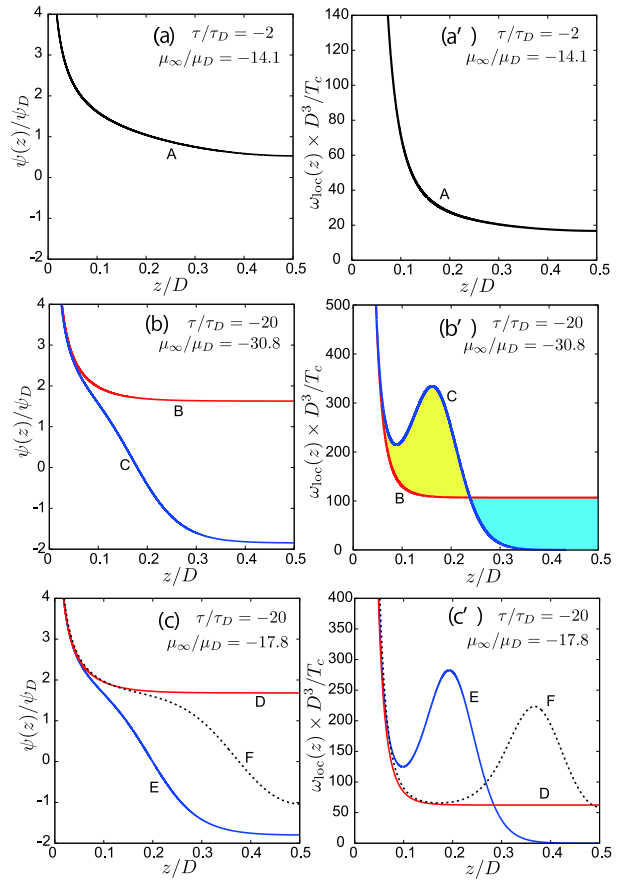


FIG. 1: (Color online) Normalized 1d profiles $\psi(z)/\psi_D$ (left) and $\omega_{loc}(z)D^3/T_c$ (right) vs z/D for $(\tau/\tau_D, \mu_\infty/\mu_D) = (-2, -14.1)$ (top), $(-20, -30.8)$ (middle), and $(-20, -17.8)$ (bottom). Top: Adsorption-dominated profile A with $\psi(z) > 0$. Middle: Two profiles B and C on the capillary condensation line with the same grand potential Ω . In (b'), the two curves of $\omega_{loc}(z)$ enclose two regions with the same area close to the surface tension σ . Bottom: Three profiles D, E, and F with the same τ and μ_∞ (see Fig.3). In (c'), Ω increases in the order of D, E, and F.

is supposed to much exceed D . The fluid is close to the bulk criticality and above the prewetting transition line [1, 4, 6, 7]. We use our local functional theory, neglecting the two-dimensional thermal fluctuations with sizes exceeding D in the xy plane.

We scale τ and ψ in units of $\tau_D \propto D^{-1/\nu}$ and $\psi_D \propto D^{-\beta/\nu}$, respectively, defined by

$$\tau_D = (\xi_0/D)^{1/\nu}, \quad (2.18)$$

$$\psi_D = (24^{\beta/\nu}/3u^*C_1\xi_0)^{1/2}\tau_D^\beta. \quad (2.19)$$

In equilibrium theory, it is convenient to assume that the fluid between the walls is in contact with a large reservoir containing the same binary mixture, where the order parameter is ψ_∞ and the chemical potential is

$$\mu_\infty = \mu(\psi_\infty, \tau). \quad (2.20)$$

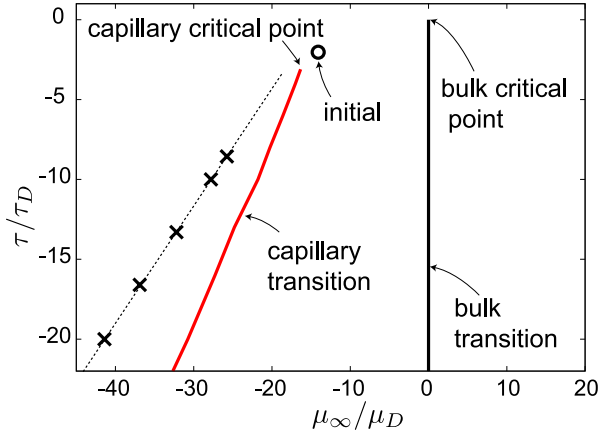


FIG. 2: (Color online) Phase diagram of a near-critical fluid in a film for large adsorption in the μ_∞/μ_D - τ/τ_D plane. The bulk coexistence line is given by $\tau < 0$ and $\mu_\infty = 0$. On its left, there appears a first-order capillary condensation line (red bold line) ending at a film critical point, which is calculated from 1d profiles. Displayed also are values of μ_∞/μ_D in steady two-phase coexistence in our simulation of a $2D \times 2D \times D$ system (\times). Starting point of our simulation ($t < 0$) is also shown (\circ).

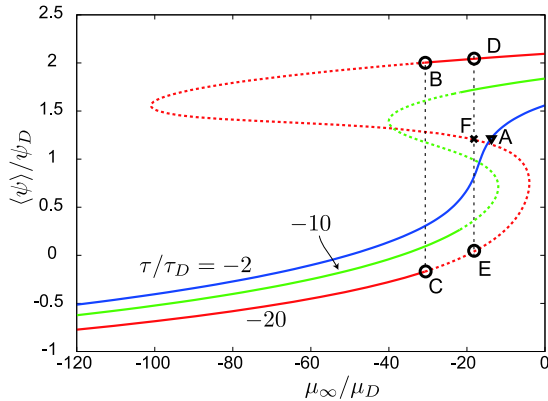


FIG. 3: (Color online) Isothermal curves in the μ_∞/μ_D - $\langle \psi \rangle/\psi_D$ plane, which are calculated for 1d profiles at $\tau/\tau_D = -2$, -10 , and -20 . For τ less than its film critical value ($= -3.14\tau_D$), a van der Waals loop appears. Dotted parts of the curves for $\tau/\tau_D = -10$ and -20 are not stable in contact with a reservoir. Points A,B,C,D,E, and F correspond to the curves in Fig.1.

Here, μ_∞ corresponds to magnetic field h for films of Ising spin systems. We are interested in the case $\mu_\infty < 0$ (or $\psi_\infty < 0$) and $\psi_0 > 0$, where ψ_0 is the value of ψ at the walls. If equilibrium is attained in the total system including the reservoir, we should minimize the film grand potential Ω . Including the surface free energy, we assume the form,

$$\Omega = \int d\mathbf{r} \omega_{\text{loc}} - T_c \int dS h_1 \psi, \quad (2.21)$$

where the space integral $\int d\mathbf{r}$ is within the film, the surface integral $\int dS$ is on the walls at $z = 0$ and D , and h_1 is a surface field symmetrically given on the two walls. In addition, we neglect the surface free energy of the form $\int dS \lambda^{-1} \psi^2$ assumed in the literature[4–7] (or we consider the limit $\lambda \rightarrow \infty$).

In Eq.(2.21) ω_{loc} is the local grand potential density including the gradient part,

$$\omega_{\text{loc}} = \omega_s + \frac{1}{2} T_c C |\nabla \psi|^2, \quad (2.22)$$

where ω_s is the excess grand potential density written as

$$\omega_s = f(\psi) - f(\psi_\infty) - \mu_\infty(\psi - \psi_\infty). \quad (2.23)$$

Now minimization of Ω yields the bulk equation,

$$\frac{\delta F}{\delta \psi} = \mu - \frac{T_c}{2} C' |\nabla \psi|^2 - T_c C \nabla^2 \psi = \mu_\infty, \quad (2.24)$$

where $C' = \partial C / \partial \psi$. The boundary conditions at $z = 0$ and D are given by

$$\psi'(x, y, 0) = -\psi'(x, y, D) = -h_1/C. \quad (2.25)$$

where $\psi' = \partial \psi / \partial z$.

The role of h_1 in this paper is simply to assure the strong adsorption regime $\psi_0/|\tau|^\beta \gg (C_1 \xi_0)^{-1/2}$ [10, 18, 19], where ψ_0 is the boundary value of ψ . This regime is eventually realized on approaching the criticality (however small h_1 is). In our simulation, the profile of ψ in the region $0 < z < \xi$ is nearly one-dimensional depending only on z even in two phase states (see Figs.5 and 6). It decays slowly as $(\ell_0 + z)^{-\beta/\nu}$ for $0 < z < \xi$ [8–10, 18], where ℓ_0 is a short microscopic length introduced by Rudnick and Jasnow [9]. With the gradient free energy in the form of Eq.(2.22), ℓ_0 is expressed as

$$\ell_0 \sim \xi_0 (C_1 \xi_0)^{-\nu/2\beta} \psi_0^{-\nu/\beta} \sim D (\psi_D/\psi_0)^{-\nu/\beta}, \quad (2.26)$$

in terms of ψ_0 . The excess surface adsorption of ψ in the region $0 < z < \ell_0$ is of order $\psi_0 \ell_0 \sim \psi_0^{1-\nu/\beta}$ and is negligible for large ψ_0 from $\beta/\nu \sim 2$, while that in the region $\ell_0 < z < \xi$ is of order $\xi^{1-\beta/\nu}$ for $\xi(\tau, \psi_m) < D/2$ [8–10]. In the strong-adsorption regime we calculate the average of ψ along the z axis,

$$\langle \psi \rangle = \int_0^D dz \psi / D. \quad (2.27)$$

In two-phase states, $\langle \psi \rangle$ depends on (x, y) .

From Eq.(2.25) it follows the estimation $h_1 \sim C(\psi_0) \psi_0 / \ell_0$. As $h_1/|\tau|^{\beta\delta-\nu} \rightarrow \infty$, we find

$$h_1 = \psi_0^{\delta-\nu/\beta} (B_1 + B_2 \tau \psi_0^{-1/\beta} + \dots), \quad (2.28)$$

where B_1 and B_2 are positive constants. This is the expression for $D \rightarrow \infty$. In this regime, the surface free energy in Eq.(2.21) is given by $-2B_1 \psi_0^{2\nu/\beta} A$, where $A = L^2$ is the surface area. In our previous paper[18], we examined the film phase behavior at fixed large ψ_0 , treating the surface free energy as a constant. In our simulation, we assume the boundary condition (2.25) with $h_1/C = 1011 \psi_D/D$ to obtain $\psi_0/\psi_D \cong 14.8$.

E. Capillary condensation transition

We consider the capillary condensation transition on the basis of one-dimensional (1d) profiles $\psi = \psi(z)$. From Eq.(2.25), we have the symmetry $\psi(z) = \psi(D - z)$. In the region $0 < z < D/2$, Eq.(2.24) is integrated to give

$$z = \int_{\psi}^{\psi_0} d\psi \left[\frac{C(\psi)/2}{\omega_s(\psi) + \Pi} \right]^{1/2}. \quad (2.29)$$

Here, $\Pi = -A^{-1}\partial\Omega/\partial D$ is the osmotic pressure. It is the force density per unit area exerted by the fluid to the plates. In our case, $\Pi < 0$, indicating attractive inter-wall interaction. In the 1d case, it is also written as

$$\begin{aligned} \Pi &= f(\psi_\infty) - f(\psi_m) - \mu_\infty(\psi_\infty - \psi_m) \\ &= -\omega_s(\psi_m). \end{aligned} \quad (2.30)$$

At the midpoint $z = D/2$, we set $\psi_m = \psi(D/2)$. The fluid at the midpoint can be in the phase favored by the walls with $\psi_m \sim \psi_{\text{cx}}$ due to the strong adsorption on the walls or in the disfavored phase with $\psi_m \cong \psi_\infty < 0$. Equation (2.30) indicates $\Pi \cong 2\mu_\infty\psi_{\text{cx}}$ in the former case and $\Pi \cong -T_c(\psi_m - \psi_\infty)^2/2\chi_{\text{cx}} \cong 0$ in the latter case, so Π can be very different in these two cases [38].

Figure 1 displays typical 1d profiles of $\psi(z)$ from Eq.(2.29) and $\omega_{\text{loc}}(z)$ in Eq.(2.22) in the range $0 < z < D/2$, which will be needed to explain our simulation results. Here we set $(\tau/\tau_D, \psi_\infty/\psi_D, \mu_\infty/\mu_D) = (-2, -1.14, -14.1)$ (top), $(-20, -1.85, -30.8)$ (middle), and $(-20, -1.81, -17.8)$ (bottom), where μ_∞ is measured in units of

$$\mu_D = T_c/D^3\psi_D \propto D^{\nu/\beta-3}. \quad (2.31)$$

Salient features in Fig.1 are as follows. (i) In Fig.1(a), ψ is positive in the whole region with $\langle \psi \rangle / \psi_D = 1.20$. (ii) In Figs.1(b) and (b'), the fluid is on the capillary condensation line, where we give two equilibrium profiles B and C with the same Ω . Here, B represents an adsorption-dominated state with $\psi_m \sim \psi_{\text{cx}}$ and $\langle \psi \rangle / \psi_D = 1.99$, while for C the film center is occupied by the disfavored phase with $\psi_m \sim -\psi_{\text{cx}}$ and $\langle \psi \rangle / \psi_D = 0.187$. In the right panel (b'), the integral of $\omega_{\text{loc}}(z)$ in the region $0 < z < D/2$ is the same for B and C. The enclosed two regions have the same area 24.7 in units of T_c/D^2 , which is close to the surface tension $\sigma = 29.2T_c/D^2$ at this τ . In addition, $\Pi \sim -\sigma/D$ for B and $\Pi \cong 0$ for C [38]. (iii) In Figs.1(c) and (c'), the parameters are those slightly below the capillary condensation line (in Fig.2 below). Here, there are three solutions with the common τ and μ_∞ , but $\langle \psi \rangle / \psi_D$ is 2.03 for (D), 0.028 for (E), and 1.20 for (F) (see Fig.3 below). If we perform simulation in contact with a reservoir with these τ and μ_∞ , the profile D is realized at long times. In the very early stage of our simulation, the dynamics is one-dimensional and the profile F is approached after quenching from A in Fig.1(a) (see Fig.7 below).

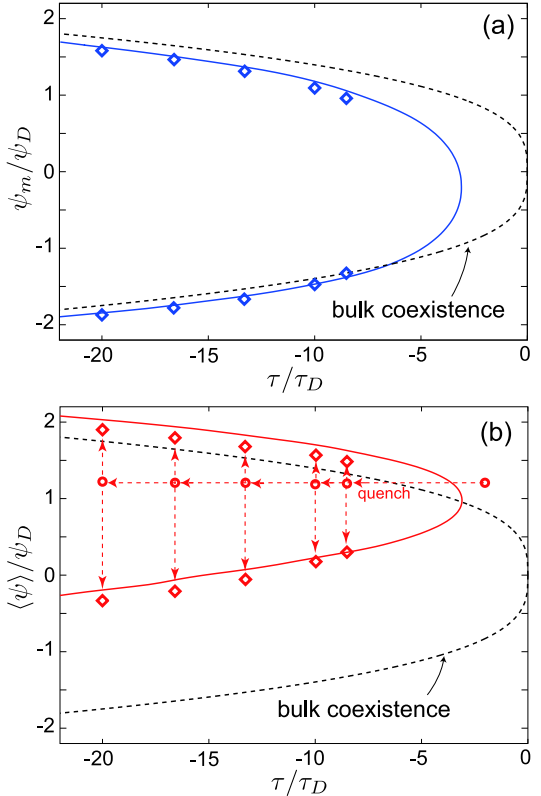


FIG. 4: (Color online) Phase diagrams in the τ/τ_D - ψ_m/ψ_D plane in (a) and in the τ/τ_D - $\langle \psi \rangle / \psi_D$ plane in (b), where ψ_m is the midpoint value. In (a) and (b), the capillary condensation curves (bold lines) are calculated from 1d profiles, where points for five τ/τ_D are those along the z axis with $(x, y) = (D, D)$ and $(D, 0)$ in the final two-phase states in our simulation (see Figs.4 and 5). Bulk coexistence curve is in broken line. In (b) our phase separation process is illustrated by arrows, where the total order parameter is conserved.

In Fig.2, we show the capillary condensation line (CCL) from 1d profiles located on the left of the bulk coexistence line in the $\tau-\mu_\infty$ plane. In our previous paper [18], the corresponding phase diagram was displayed in the $\tau-\psi_\infty$ plane. The discontinuities of the physical quantities across CCL increase with increasing $|\tau|$ vanishing at a film critical point. At this film criticality, τ , ψ_∞ , and μ_∞ are calculated as

$$\left(\frac{\tau}{\tau_D}, \frac{\psi_\infty}{\psi_D}, \frac{\mu_\infty}{\mu_D} \right) = (-3.14, -1.27, -16.3), \quad (2.32)$$

where we also have $\langle \psi \rangle / \psi_D = 0.989$ and $\psi_m / \psi_D = -0.173$. Hereafter, the chemical potential μ_∞ on this CCL will be written as $\mu_{\text{cx}}^{\text{ca}}(\tau)$. Our numerically calculated CCL is well fitted to the linear form,

$$\mu_{\text{cx}}^{\text{ca}}(\tau) / \mu_D + 16.3 \cong 0.86(\tau/\tau_D + 3.14). \quad (2.33)$$

In Fig.1(b'), the two areas enclosed by the two curves of $\omega_{\text{loc}}D^3/T_c$ are the same ($\sim \sigma D^2/T_c$). Thus, for

TABLE I: Values of μ_∞/μ_D from our simulation in a finite $2D \times 2D \times D$ system for five τ/τ_D . The corresponding values of $\mu_{\text{cx}}^{\text{ca}}/\mu_D$ on the CCL from 1d profiles are also shown.

τ/τ_D	-8.5	-10	-13.3	-16.6	-20
μ_∞/μ_D (finite)	-25.8	-27.8	-32.2	-36.6	-41.4
$\mu_{\text{cx}}^{\text{ca}}/\mu_D$ (1d)	-20.6	-21.8	-24.9	-27.7	-30.8

$|\tau|/\tau_D \gg 1$, the surface tension σ and the free energy difference per unit area $-2\mu_{\text{cx}}^{\text{ca}}\psi_{\text{cx}}D$ are of the same order. See the sentences below Eq.(2.30) and the explanation of Fig.1(b'). For $|\tau| \gg \tau_D$, it follows the relation,

$$\mu_{\text{cx}}^{\text{ca}} \sim -\sigma/\psi_{\text{cx}}D \sim -|\tau/\tau_D|^{2\nu-\beta} \mu_D. \quad (2.34)$$

Since $2\nu - \beta \cong 0.94$, the theoretical formula (2.34) is consistent with the numerical formula (2.33). Note that Eq.(2.34) is equivalent to the Kelvin equation known for the gas-liquid transition in pores [1, 2].

We have already presented a special case of three 1d profiles in Fig.1(c) for $(\tau/\tau_D, \mu_\infty/\mu_D) = (-20, -17.8)$. In Fig.3, we show isothermal curves in the μ_∞ - $\langle\psi\rangle$ plane, which are calculated from 1d profiles with $\tau/\tau_D = -2, -10$, and -20 . The relation between μ_∞ and $\langle\psi\rangle$ is monotonic for $\tau/\tau_D \geq -3.14$ (above the film critical temperature), while it exhibits a van der Waals loop for $\tau/\tau_D < -3.14$ with three 1d states in a window range $\mu_{\infty 1} < \mu_\infty < \mu_{\infty 2}$ [39]. Here, $\mu_{\infty 1}$ and $\mu_{\infty 2}$ coincide at the film criticality. The isotherms consist of stable and unstable parts characterized by the sign of the film susceptibility defined by

$$\chi_{\text{film}} = T_c(\partial\langle\psi\rangle/\partial\mu_\infty)_\tau. \quad (2.35)$$

In Fig.3, points A,B,C,D,E, and F correspond to the curves in Fig.1. Dotted parts of the two curves of $\tau/\tau_D = -10$ and -20 are not stable in the presence of a mass current from a reservoir with common μ_∞ .

Previously, some authors [13, 14] calculated the stable parts of isotherms of the average density in the film versus the chemical potential. In our local functional theory, the three 1d profiles can be calculated since a unique profile follows for any given set of τ and $\langle\psi\rangle$. In equilibrium fluctuation theory of films [1], χ_{film} is proportional to the variance of the order parameter fluctuations, so its negativity indicates thermodynamic instability.

Furthermore, Fig.4 gives the phase diagrams in the τ - ψ_m and τ - $\langle\psi\rangle$ planes. Bold lines represent the capillary condensation curve from 1d profiles as in Fig.2. In steady two-phase states in our simulation, ψ_m and $\langle\psi\rangle$ depend on x and y , so points for five τ represent $\psi_m(x, y) = \psi(x, y, D/2)$ and $\langle\psi\rangle(x, y)$ with $(x, y) = (D, D)$ and $(D, 0)$ (see Figs.5 and 6). The former line passes through a domain of the phase disfavored by the walls and the latter through the favored phase only. Phase diagrams similar to Fig.4(b) have been obtained in experiments of the capillary condensation in porous media [2].

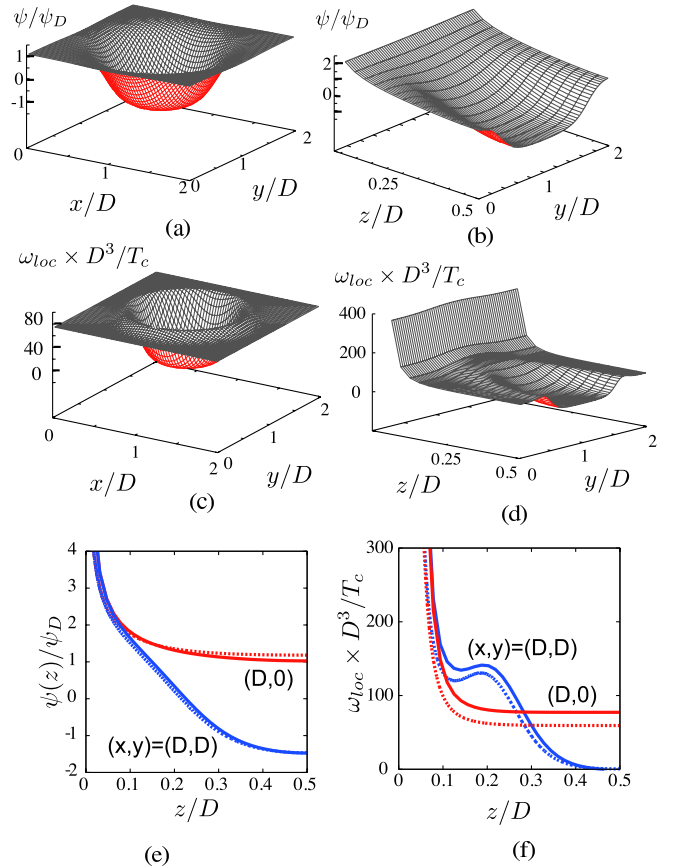


FIG. 5: (Color online) Equilibrium two-phase state at $\tau/\tau_D = -10$ in a $2D \times 2D \times D$ system: ψ/ψ_D (top) and $\omega_{\text{loc}}D^3/T_c$ (middle) in the xy plane at $z = D/2$ (left) and in the yz plane at $x = D$ (right). Bottom: ψ/ψ_D (left) and $\omega_{\text{loc}}D^3/T_c$ (right) along the z axis for $(x, y) = (D, D)$ (blue bold line) and $(D, 0)$ (red bold line), while dotted lines represent 1d profiles from Eq.(2.29).

III. PHASE SEPARATION DYNAMICS

We performed simulation of phase separation in a $L \times L \times D$ cell with $L = 2D$ imposing the periodic boundary condition along the x and y axes. In this section, we describe phase separation realized for deep quenching. However, it was not realized for shallow quenching ($|\tau|/\tau_D \lesssim 7$), for which χ_{film} in Eq.(2.35) is positive.

A. Dynamic equations and simulation method

Supposing an incompressible fluid binary mixture with a homogeneous temperature, we use the model H equations [24, 25, 40]. The order parameter ψ is a conserved variable governed by

$$\frac{\partial\psi}{\partial t} = -\nabla \cdot (\psi\mathbf{v}) + \lambda\nabla^2 \frac{\delta F}{\delta\psi}, \quad (3.1)$$

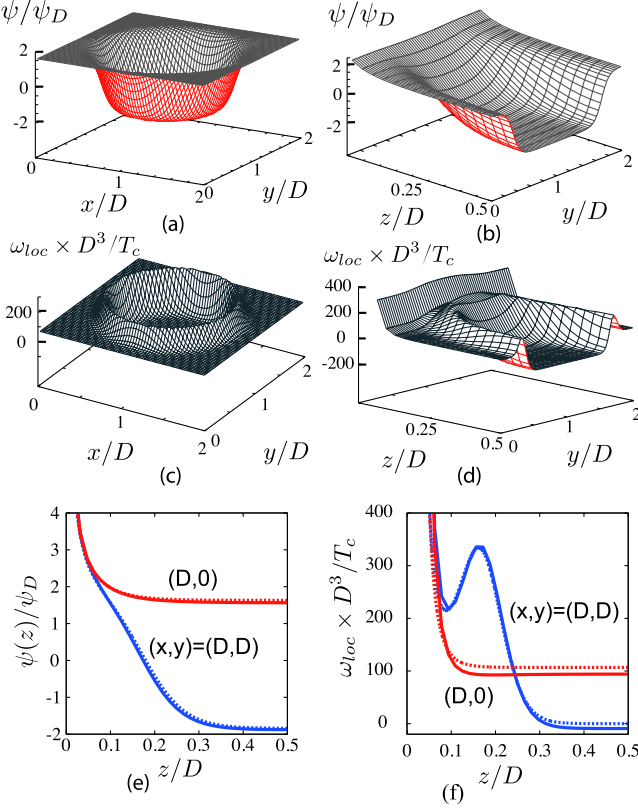


FIG. 6: (Color online) Equilibrium two-phase state at $\tau/\tau_D = -20$ in a $2D \times 2D \times D$ system: ψ/ψ_D (top) and $\omega_{loc} D^3/T_c$ (middle) in the xy plane at $z = D/2$ (left) and in the yz plane at $x = D$ (right). Bottom: ψ/ψ_D (left) and $\omega_{loc} D^3/T_c$ (right) along the z axis for $(x, y) = (D, D)$ (blue bold line) and $(D, 0)$ (red bold line), which are closer to the 1d profiles (dotted lines) from Eq.(2.29) than in Fig.5.

where λ is the kinetic coefficient and the functional derivative $\delta F/\delta\psi$ may be calculated from Eq.(2.4) with the aid of Eqs.(2.10), (2.15), and (2.16) outside and inside CX. We neglect the random source term originally present in critical dynamics [24, 25], because we treat the deviations much larger than the thermal fluctuations. The velocity field \mathbf{v} satisfies $\nabla \cdot \mathbf{v} = 0$ and vanishes at $z = 0$ and D . In the Stokes approximation[40], \mathbf{v} is determined by

$$\bar{\eta} \nabla^2 \mathbf{v} = \nabla p_0 + \psi \nabla (\delta F/\delta\psi), \quad (3.2)$$

where $\bar{\eta}$ is the shear viscosity and the role of a pressure p_0 is to ensure $\nabla \cdot \mathbf{v} = 0$. See Appendix for the expression of the stress tensor in near-critical fluids and the derivation of Eq.(3.2).

The kinetic coefficients λ and $\bar{\eta}$ should be treated as renormalized ones [24, 25, 40] (see the last sentence of Subsec.IIA). In the vicinity of the bulk coexistence curve, λ may be approximated by

$$\lambda = \chi_{cx} D_\xi / T_c, \quad (3.3)$$

where χ_{cx} is the susceptibility on CX in Eq.(2.13) and D_ξ is the mutual diffusion constant of the Stokes form,

$$D_\xi = T_c / 6\pi\bar{\eta}\xi, \quad (3.4)$$

with $\xi = \xi'_0 |\tau|^{-\nu}$ being the correlation length on CX. In our simulation, $|\psi|$ is of order ψ_{cx} at $z = D/2$ (see Figs.5 and 6 below), which supports Eqs.(3.3) and (3.4). The viscosity $\bar{\eta}$ exhibits a very weak critical singularity and may be treated as a constant independent of τ .

In this paper, we also performed simulation for model B without the hydrodynamic interaction [24], where ψ obeys the diffusive equation,

$$\frac{\partial \psi}{\partial t} = \lambda \nabla^2 \frac{\delta F}{\delta \psi}. \quad (3.5)$$

The kinetic coefficient λ is assumed to be given by Eqs.(3.3) and (3.4) as in the model H case. Then, comparing the results from the two models, we can examine the role of the hydrodynamic interaction in phase separation. Model B has been used to investigate surface-directed phase separation in binary alloys [31].

In integrating Eqs.(3.1) and (3.5), the mesh length was $\Delta x = D/32$ and the time interval width was $\Delta t = 2 \times 10^{-6} t_0$. The initial state was the 1d profile A in Fig.1(a) at $\tau/\tau_D = -2$ with small random numbers ($\sim 10^{-4}$) superimposed at the mesh points. At $t = 0$, we decreased τ to a final reduced temperature. For $t > 0$, there was no mass exchange between the film and the reservoir so that the total order parameter $\int d\mathbf{r} \psi$ was fixed at $1.20\psi_D D L^2$. We will measure time after quenching in units of

$$t_0 = D^2/D_\xi, \quad (3.6)$$

which is the mutual diffusion time in the film assumed to be much longer than the thermal diffusion time. We note that the natural time unit in bulk phase separation has been the order parameter relaxation time $t_\xi = \xi^2/D_\xi$ [25, 40, 41]. Here, $t_0/t_\xi = (D/\xi)^2 = R_\xi^2 |\tau/\tau_D|^{2\nu} \sim 100$ for $|\tau/\tau_D| \sim 10$.

B. Steady two-phase states

For sufficiently deep quenching, we realized phase separation to find a steady two-phase state at long times both for model H and model B. We could also calculate this final state more accurately from the following relaxation-type equation,

$$\frac{\partial \psi}{\partial t} = -L_0 \left[\frac{\delta F}{\delta \psi} - \left\langle \frac{\delta F}{\delta \psi} \right\rangle_t \right], \quad (3.7)$$

where L_0 is a constant and $\langle \delta F/\delta\psi \rangle_t$ is the space average of $\delta F/\delta\psi$ at time t . Because of its simplicity, we integrated Eq.(3.7) with a fine mesh length of $\Delta x = D/64$. The data points in Figs.2 and 4 and the snapshots in Figs.5 and 6 are those from the steady states of Eq.(3.7).

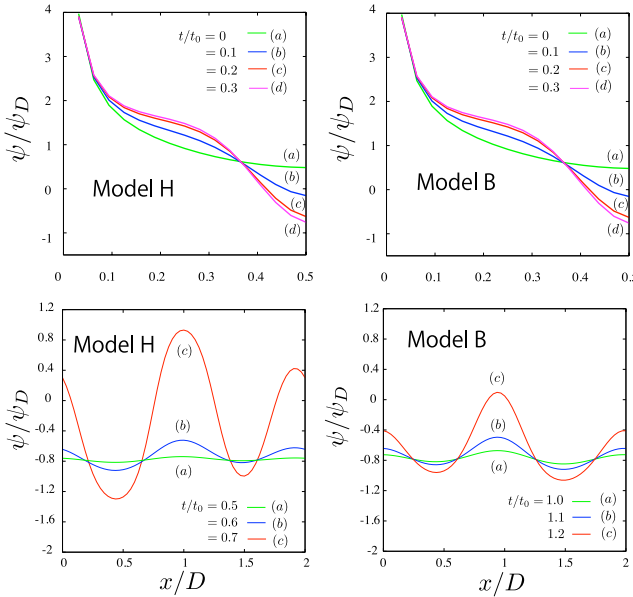


FIG. 7: (Color online) Early-stage time-evolution of ψ/ψ_D for model H (left) and model B (right) after quenching from the profile A in Fig.1(a) to $\tau/\tau_D = -20$. Shown are the profiles along the z axis for $(x, y) = (D, D)$ at $t/t_0 = 0, 0.1, 0.2$, and 0.3 (top) and along the x axis for $(y, z) = (1.5D, 0.5D)$ (bottom) at later times. In the top panels, the profile F in Fig.1(c) is approached without noticeable differences between the two models. In the bottom panels, fluctuations in the xy plane appear and coarsening is much quickened for model H than for model B, where $t/t_0 = 0.5, 0.6$, and 0.7 for model H and $1.0, 1.1$, and 1.2 for model B.

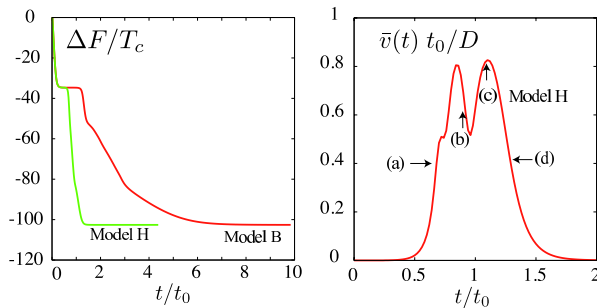


FIG. 8: (Color online) Time-evolution of the normalized free energy decrease $\Delta F(t)/T_c$ for model H and model B (left) and $\bar{v}(t)t_0/D$ for model H (right) after quenching from the profile A in Fig.1(a). At points (a), (b), (c), and (d) (right) snapshots of ψ and \mathbf{v} will be given in Fig.9.

In Fig.4, the deviations of ψ_m and $\langle\psi\rangle$ from those on CCL are surprisingly small, though the lateral dimension L is only $2D$. However, in Table 1, the final two-phase values of μ_∞ considerably deviate from those on CCL. This may be ascribed to the relatively small size of the susceptibility χ_{cx} for these cases. That is, if we set $\chi_{cx} = A_\chi^{-1} T_c \psi_D / \mu_D$ on CX, we obtain $A_\chi = 120$ and 283 for $\tau/\tau_D = -10$ and -20 , respectively. Here, if we multiply

the deviation of ψ_m/ψ_D or $\langle\psi\rangle/\psi_D$ by of A_χ , we obtain that of μ_∞/μ_D .

In Figs.5 and 6, we display the final profiles of ψ and ω_{loc} in the xy plane at $z = D/2$ (left) and in the zy plane at $x = D$ (right) for $\tau/\tau_D = -10$ and -20 . In these cases, ξ on CX is $0.078D$ and $0.051D$, respectively, which is of the order of the interface thickness. Displayed in the bottom panels are 1d profiles of ψ and ω_{loc} along the z axis for the two lateral points $(x, y) = (D, D)$ and $(D, 0)$. These profiles are rather close to the 1d profiles from Eq.(2.29) in accord with Fig.4.

C. Time evolution

Both for model H and model B, early-stage time-evolution proceeds as follows. Just after quenching, ψ changes only along the z axis to approach the 1d profile at the final τ with fixed $\langle\psi\rangle$ (see Fig.3). If this 1d profile satisfies the instability condition $\chi_{film} < 0$, it follows 3d spinodal decomposition. On the other hand, if it satisfies the stability condition $\chi_{film} > 0$, it remains stationary in simulation without thermal noise.

Figure 7 displays ψ after quenching to $\tau/\tau_D = -20$. In the top panels, it is plotted along the z axis with $(x, y) = (D, D)$ at $t/t_0 = 0, 0.1, 0.2$, and 0.3 . The velocity field nearly vanishes for model H, so there is almost no difference between the results of these models. However, in the bottom panels, the 1d profile becomes unstable with respect to the fluctuations varying in the xy plane for $t/t_0 \gtrsim 0.5$. The velocity field grows gradually for model H. In this second time range, the domain formation is much quicker for model H than for model B.

In the left panel of Fig.8, we show the free energy decrease $\Delta F = F(t) - F(+0)$ at $\tau/\tau_D = -20$ as a function of t for model H and model B. Here, $F(t)$ is the total bulk free energy in Eq.(2.4) with $F(+0)$ being its value just after quenching. Its decrease is accelerated with development of the fluctuations in the xy plane. The coarsening is slower for model B than for model H by about 5 times. In the right panel of Fig.8, we show the characteristic velocity amplitude $\bar{v}(t)$ for model H, which is defined by

$$\bar{v}(t)^2 = \int d\mathbf{r} |\mathbf{v}|^2 / DL^2. \quad (3.8)$$

For $\tau/\tau_D = -20$, $\bar{v}(t)$ is equal to $0.021, 0.106$, and 0.485 at $t/t_0 = 0.5, 0.6$, and 0.7 , respectively, increasing up to 0.8 , in units of D/t_0 .

In Fig.9, we show late stage snapshots of ψ and \mathbf{v} in the xz plane (top) and in the xy plane (middle) for $\tau/\tau_D = -20$ for model H, where t/t_0 is equal to (a) 0.7 , (b) 0.9 , (c) 1.1 , and (d) 1.3 after quenching. In (a) we can see a network-like domain of the disfavored phase. In (b) three domains can be seen, where the middle one is being absorbed into the bottom one, soon resulting in two domains at $t/t_0 \sim 1.0$. This process gives rise to a dip in $\bar{v}(t)$ in Fig.8(b) since these two domains are considerably apart. In (c) and (d), furthermore, coalescence of

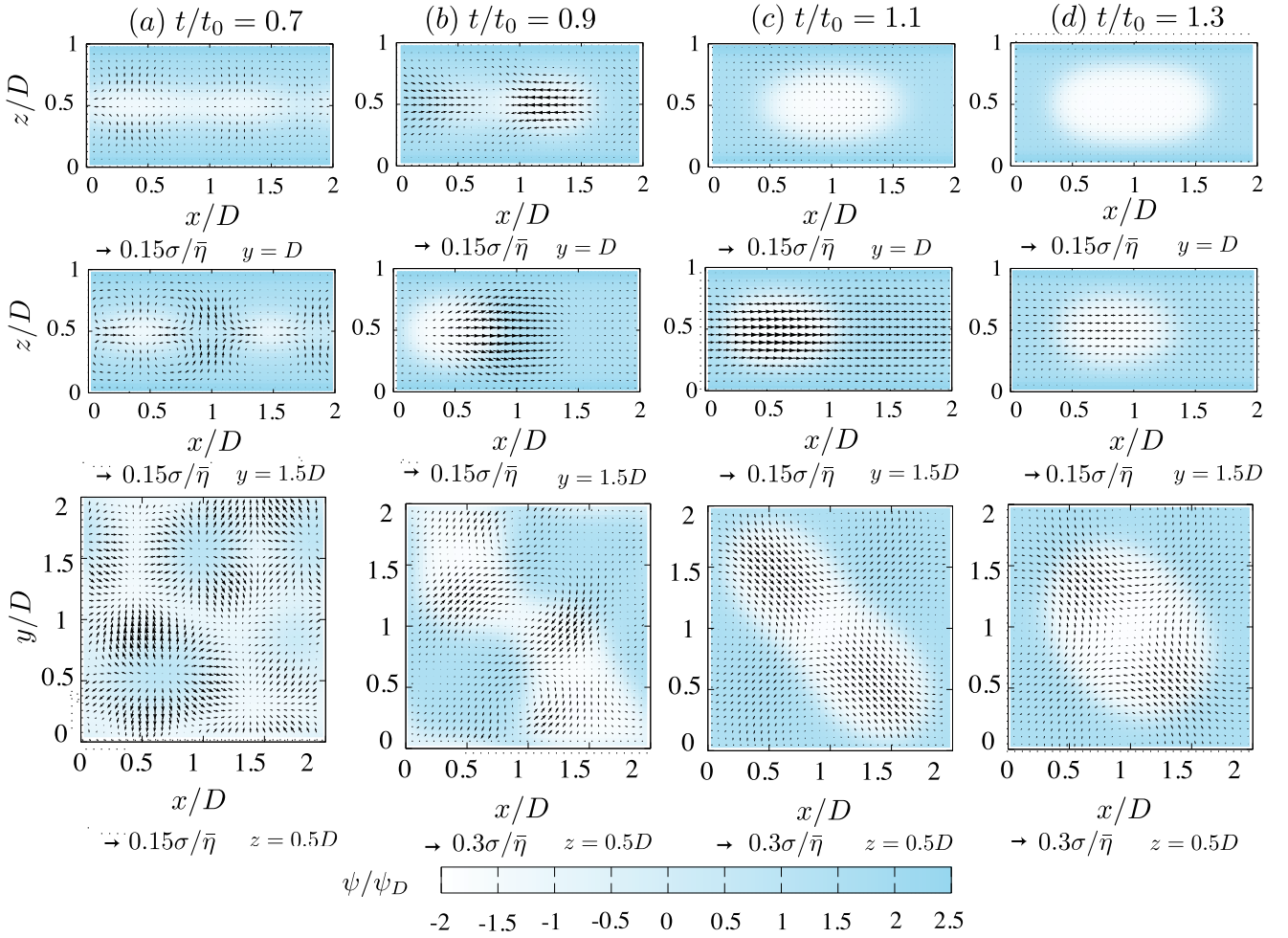


FIG. 9: (Color online) Cross-sectional velocity field \mathbf{v} (arrows) and order parameter ψ (in gradation according the color bar) in phase separation for $\tau/\tau_D = -20$ in model H, where t/t_0 is equal to (a) 0.7, (b) 0.9, (c) 1.1, and (d) 1.3 after quenching. Displayed are (v_x, v_z) and ψ in the xz plane at $y = D$ (top), those at $y = 1.5D$ (middle), and (v_x, v_y) and ψ in the xy plane at $z = D/2$ (bottom). Arrows below panels indicate typical magnitudes of the velocities, where σ is the surface tension and $\bar{\eta}$ is the shear viscosity. Final state is given in Fig.6.

these two domains is taking place. The arrows below the panels indicate the typical velocity, $0.15\sigma/\bar{\eta}$ or $0.3\sigma/\bar{\eta}$, where σ is the surface tension and $\bar{\eta}$ is the shear viscosity. Note that the typical velocity in the late-stage bulk spinodal decomposition is given by $v_c = 0.1\sigma/\bar{\eta}$ [25, 41], which follows from the stress balance $\sigma/R \sim 6\pi\bar{\eta}v_c/R$ with $R \sim v_{ct}$ being the typical domain length. In our case, from Eq.(2.17) these velocities are related as

$$D/t_0 = T_c/6\pi\bar{\eta}\xi D = (\xi/6\pi A_\sigma D)(\sigma/\bar{\eta}). \quad (3.9)$$

Thus, $D/t_0 = 0.036\sigma/\bar{\eta}$ for $\tau/\tau_D = -20$ in Fig.9.

IV. SUMMARY AND REMARKS

In summary, we have examined the phase separation in a near-critical binary mixture between symmetric parallel

plates in the strong adsorption regime around the capillary condensation line (CCL). Using model H and model B, simulation has been performed in a $2D \times 2D \times D$ cell. We summarize our main results.

(i) In Sec.II, we have presented the singular free energy with the gradient part outside and inside the bulk coexistence curve. Applying it to near-critical fluids between parallel plates, typical 1d profiles have been given in Fig.1. CCL has been plotted in the $\tau-\mu_\infty$ plane in Fig.2. The points for the steady two-phase states from our simulation are located in the left side of CCL. In Fig.3, we have also found the van der Waals loop of isothermal curves in the $\langle\psi\rangle-\mu_\infty$ plane, where τ is smaller than the film critical value. The phase diagrams have been plotted in the $\tau-\psi_m$ and $\tau-\langle\psi\rangle$ planes in 3d (bulk) and 2d (film) in Fig.4. The Kelvin relation (2.34) has also been obtained, since the osmotic pressure Π is of order $-\sigma/D$ right below CCL [38].

(ii) In Sec.III, we have first displayed the cross-sectional profiles of ψ and ω_{loc} in steady two-phase states in Figs.5 and 6. The profiles along z axis for $(x, y) = (D, D)$ and $(D, 0)$ closely resemble the corresponding 1d profiles. For quenching to $\tau/\tau_D = -20$, we have examined time-evolution of ψ . It occurs only along the z axis in the very early stage in the top panels of Fig.7, where there is no difference between the results of model H and model B. Subsequently, inhomogeneities appear in the xy plane. The free energy decrease $\Delta F(t) = F(t) - F(+0)$ and the typical velocity amplitude $\bar{v}(t)$ defined in Eq.(3.8) have been plotted in Fig.8. The velocity field considerably quicken the interface formation and the coarsening for model H than for model B. Profiles of ψ and \mathbf{v} in the late stage coarsening due to the flow have been presented in Fig.9, where the domain coalescence can be seen and the maximum velocity is of order $0.1\sigma/\bar{\eta}$ as in bulk spinodal decomposition [41].

We make some remarks.

1) In the static part of our theory, we neglect the thermal fluctuations varying in the lateral directions with wavelengths longer than D . Thus this 2d transition exhibits mean-field behavior. In fact, the curves of ψ_m vs τ and $\langle \psi \rangle$ vs τ are parabolic near the film criticality in Fig.4.

2) In our simulation, we soon have only two or three domains in the cell as in the bottom panels of Fig.9. The lateral dimension $L = 2D$ in this paper is too short to investigate the domain growth law in the xy plane. Simulation with larger L/D should be performed in future.

3) From the van der Waals loop of the isothermal curves in the $\langle \psi \rangle$ - μ_∞ plane in Fig.3, we may predict how phase separation proceeds after quenching. We have examined phase separation via spinodal decomposition. However, in real experiments, phase separation may occur via nucleation for metastable 1d profiles. Note that hysteretic behavior has been observed in phase-separating fluids in pores and has not been well explained [1, 2, 26, 27].

4) In a number of experiments and simulations of surface-directed phase separation [29, 33, 34], composition waves along the z axis have been observed near the wall in the early stage. In these cases, the degree of adsorption has changed appreciably upon quenching. In the strong adsorption regime in this paper, 1d dynamics occurs in the initial stage, but there are no composition waves as in the top panels of Fig.7.

5) The static part of this work is applicable to any Ising-like near-critical systems and can readily be generalized to n -component spin systems. In the dynamics, we have used model H with a homogeneous temperature and incompressible flows. On the other hand, in one-component near-critical fluids, the latent heat released or absorbed at the interfaces gives rise to significant hydrodynamic flow because of the enhanced isobaric thermal expansion [25, 42]. Also promising in future should be extension of this work to near-critical fluids in porous media.

Acknowledgments

This work was supported by Grant-in-Aid for Scientific Research from the Ministry of Education, Culture, Sports, Science and Technology of Japan. S. Y. was supported by the Japan Society for Promotion of Science. A.O. would like to thank Sanjay Puri for informative correspondence.

Appendix: Stress tensor in near-critical fluids

In near-critical fluids, we treat slow flows with low Reynolds numbers. The total (reversible) stress tensor is given by $p_0\delta_{ij} + \Pi_{\psi ij}$, where p_0 is nearly homogeneous throughout the film and the reservoir. The $\Pi_{\psi ij}$ is the stress tensor due to the composition deviation[25],

$$\Pi_{\psi ij} = p_\psi \delta_{ij} + C(\nabla_i \psi)(\nabla_j \psi), \quad (\text{A1})$$

where $\nabla_i = \partial/\partial x_i$. The diagonal part p_ψ is written as

$$\begin{aligned} p_\psi &= \psi\mu - f - \frac{1}{2}(C + C'\psi)|\nabla\psi|^2 - C\psi\nabla^2\psi \\ &= \psi(\delta F/\delta\psi) - f - C|\nabla\psi|^2/2, \end{aligned} \quad (\text{A2})$$

where $C' = \partial C/\partial\phi$. The second part in Eq.(A1) contains off-diagonal components relevant for curved interfaces. In deriving Eq.(3.2), we use the relation,

$$\sum_j \nabla_j \Pi_{\psi ij} = \psi \nabla_i (\delta F/\delta\psi). \quad (\text{A3})$$

-
- [1] R. Evans and U. M. B. Marconi, J. Chem. Phys. **86**, 7138 (1987); R. Evans, J. Phys.: Condens. Matter **2**, 8989 (1990).
 - [2] L.D. Gelb, K.E. Gubbins, R. Radhakrishnan, and M. Sliwinska-Bartkowiak, Rep. Prog. Phys. **62**, 1573 (1999).
 - [3] K. Binder, D. Landau, and M. Müller, J. Stat. Phys. **110**, 1411 (2003); M. Müller and K. Binder, J. Phys.: Condens. Matter **17**, S333 (2005); K. Binder, J. Horbach, R. Vink, and A. De Virgiliis, Soft Matter, **4**, 1555 (2008).
 - [4] J. W. Cahn, J. Chem. Phys. **66** 3667 (1977).
 - [5] K. Binder, in *Phase Transitions and Critical Phenomena*, C. Domb and J. L. Lebowitz, eds. (Academic, London, 1983), Vol. 8, p. 1.
 - [6] P.G. de Gennes, Rev. Mod. Phys. **57**, 827 (1985).
 - [7] D. Bonn and D. Ross, Rep. Prog. Phys. **64**, 1085 (2001).
 - [8] B. M. Law, Prog. Surf. Sci. **66**, 159 (2001).
 - [9] J. Rudnick and D. Jasnow, Phys. Rev. Lett. **48**, 1059 (1982); ibid. **49**, 1595 (1982)

- [10] A. J. Liu and M. E. Fisher, Phys. Rev. A **40**, 7202 (1989).
- [11] M. E. Fisher and H. Nakanishi, J. Chem. Phys. **75**, 5857 (1981); H. Nakanishi and M. E. Fisher, J. Chem. Phys. **78**, 3279 (1983).
- [12] R. Evans, U. M. B. Marconi, P. Tarazona, J. Chem. Soc., Faraday Trans. **82**, 1763 (1986); P. Tarazona, U.M.B Marconi, R. Evans, Mol. Phys. **60**, 573 (1987);
- [13] B. K. Peterson, K. E. Gubbins, G. S. Heffelfinger, U. Marini, B. Marconi, and F. van Swol, J. Chem. Phys. **88**, 6487 (1988).
- [14] K. Binder and D. P. Landau, J. Chem. Phys. **96**, 1444 (1992).
- [15] For binary mixtures, we use the chemical potential difference $\mu_1 - \mu_2$ between the two components. To be precise, μ_∞ in the text is the deviation of the chemical potential difference $\mu(c_\infty, T) - \mu(c_c, T)$ around the critical composition c_c .
- [16] A. Maciołek, A. Drzewiński, and R. Evans, Phys. Rev. E **64**, 056137 (2001).
- [17] S. K. Singh, A. K. Saha, and J. K. Singh, J. Phys. Chem. B **114**, 4283 (2010).
- [18] R. Okamoto and A. Onuki, J. Chem. Phys. **136**, 114704 (2012).
- [19] M. E. Fisher and H. Au-Yang, Physica **101A**, 255 (1980).
- [20] M. E. Fisher and P. J. Upton, Phys. Rev. Lett. **65**, 3405 (1990); Z. Borjan and P. J. Upton, *ibid.* **81**, 4911 (1998); *ibid.* **101**, 125702 (2008).
- [21] A. Gambassi, A. Maciołek, C. Hertlein, U. Nellen, L. Helden, C. Bechinger, and S. Dietrich, Phys. Rev. E **80**, 061143 (2009).
- [22] S. Samin and Y. Tsori, EPL **95**, 36002 (2011).
- [23] R. Okamoto and A. Onuki, Phys. Rev. E **84**, 051401 (2011).
- [24] P.C. Hohenberg and B.I. Halperin, Rev. Mod. Phys. **49**, 435 (1977).
- [25] A. Onuki, *Phase Transition Dynamics* (Cambridge University Press, Cambridge, 2002).
- [26] M. C. Goh, W. I. Goldburg, and C. M. Knobler, Phys. Rev. Lett. **58**, 1008 (1987); A. P. Y. Wong, S. B. Kim, W. I. Goldburg, and M. H. W. Chan, *ibid.* **70**, 954 (1993).
- [27] S. B. Dierker and P. Wiltzius, Phys. Rev. Lett. **58**, 1865 (1987).
- [28] A. J. Liu, D. J. Durian, E. Herbolzheimer, and S. A. Safran, Phys. Rev. Lett. **65**, 1897 (1990).
- [29] R. A. L. Jones, L. J. Norton, E. J. Kramer, F. S. Bates, and P. Wiltzius, Phys. Rev. Lett. **66**, 1326 (1991).
- [30] H. Tanaka, Phys. Rev. Lett. **70**, 53 (1993); *ibid.* **70**, 2770 (1993); J. Phys.: Condens. Matter **13**, 4637 (2001).
- [31] S. K. Das, S. Puri, J. Horbach, and K. Binder, Phys. Rev. E **72**, 061603 (2005).
- [32] M. R. Swift, W. R. Osborn, and J.M. Yeomans, Phys. Rev. Lett. **75**, 830 (1995).
- [33] H. Tanaka and T. Araki, Europhys. Lett. **51** 154 (2000).
- [34] P. K. Jaiswal, S. Puri, and S. K. Das, Phys. Rev. E **85**, 051137 (2012); EPL, **97**, 16005 (2012).
- [35] F. Porcheron and P. A. Monson, Langmuir **21**, 3179 (2005).
- [36] P. Schofield, Phys. Rev. Lett. **22**, 606 (1969); P. Schofield, J.D. Lister, and J.T. Ho, *ibid.* **23**, 1098 (1969).
- [37] Reliable values of R_χ and R_ξ in the literature are 4.9 and 1.9, respectively[18, 25]. The correlation length and the susceptibility on CX are considerably underestimated in our theory.
- [38] The scaled quantity $\mathcal{A} \equiv -D^3 \Pi / T_c > 0$ is one of the Casimir amplitudes depending on τ/τ_D and ψ_∞/ψ_D [18]. Its value at the bulk criticality is $\mathcal{A}_{\text{critical}} = 0.558$. For $|\tau/\tau_D| \gg 1$, we obtain $\mathcal{A} \cong A_{\text{os}} |\tau/\tau_D|^{2\nu} \gg 1$ with $A_{\text{os}} \cong 2$ just below CCL (for (B) in Fig.1) and $\mathcal{A} \cong 0$ just above CCL (for (C) in Fig.1).
- [39] In Fig.13 of Ref.[18], we already found a cubic relation between ψ_m (instead of $\langle \psi \rangle$) and ψ_∞ (instead of μ_∞) near the film criticality for $\tau/\tau_D > -3.14$, which is a mean-field result due to neglect of 2d thermal fluctuations with sizes longer than D .
- [40] K. Kawasaki, Prog. Theor. Phys. **57**, 826 (1977); K. Kawasaki and T. Ohta, *ibid.* **59**, 362 (1978).
- [41] E. D. Siggia, Phys. Rev. A **20**, 595 (1979).
- [42] R. Teshigawara and A. Onuki, Phys. Rev. E **82**, 021603 (2010); *ibid.* **84**, 041602 (2011).